Supplement to "Confinement of air in the Asian monsoon anticyclone and pathways of convective air to the stratosphere during summer season"

Bernard Legras and Silvia Bucci

Laboratoire de Météorologie Dynamique, UMR 8539, CNRS/PSL-ENS/Sorbonne Université/Ecole Polytechnique, Paris, France

Correspondence: Bernard Legras (bernard.legras@lmd.ens.fr)

S1 True altitude versus barometric altitude

The barometric altitude and the geopotential are both derived from the pressure and the temperature using the hydrostatic equation. The barometric altitude uses the temperature profile of the Standard Atmosphere while the geopotential altitude uses the observed temperature profile. The discrepancy between the two quantities in the Asian monsoon region is the largest over the Tibetan plateau. This is due to the strong warm anomaly in the middle and upper troposphere induced by the plateau which visualized by the drop of the isentropic surfaces in Fig. S1.

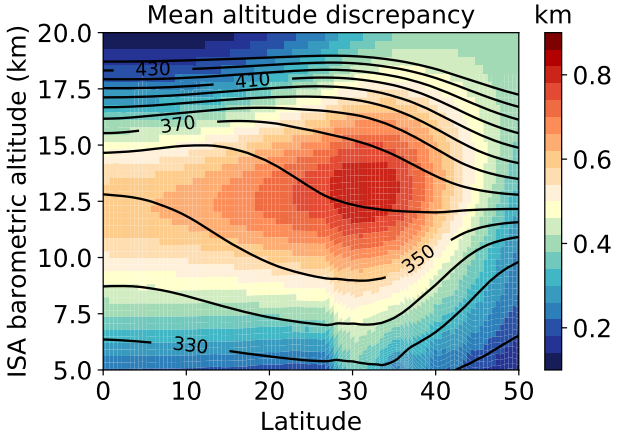

Figure S1. Difference between the geopotential altitude and the barometric altitude (in km) averaged over July-August 2017 in the 73E-97E longitude range. Thin contours show potential temperature (in K).

S2 Montgomery potential

The Montgomery potential $M = C_pT + gz$ defines the geostrophic flow on isentropic surfaces as $(fu_g = -\frac{\partial M}{\partial y},\ fv_g = \frac{\partial M}{\partial x})$. The closed contours of the average M over July and August 2017 in Fig. S2 show how air circulates around the AMA. The pattern is similar from $\theta = 350$ K to $\theta = 400$ K, indicating the barotropic structure of the flow with two centres located respectively over the Tibetan plateau and Iran, as noticed in many previous studies. At $\theta = 340$ K, the Montgomery potential exhibits a strong anticyclonic centre over Africa and Arabia, which is a pattern of the African monsoon.

Using Nakamura (1995) it is easily shown that the circulation time along a closed non singular contour of the Montgomery potential is given by

$$\tau(M) = \frac{d\mathcal{A}(M)}{dM} \tag{1}$$

where

$$\mathcal{A}(M^*) = \iint\limits_{M<M^*} f dx dy.$$

Figure S3 shows the value of τ as a function of $\mathcal{A}$ from the exterior to the interior of the AMA, as for several values of the potential temperature. The left part of the curves with $\tau < 10$ days must be discarded as it corresponds to non closed contours. The right part corresponds to the smallest contours for which the circulation time tends to zero. We see that most of the curves (from 360 K to 400 K) exhibit a plateau at about three weeks followed by a second one at about two weeks. The first plateau corresponds to contours

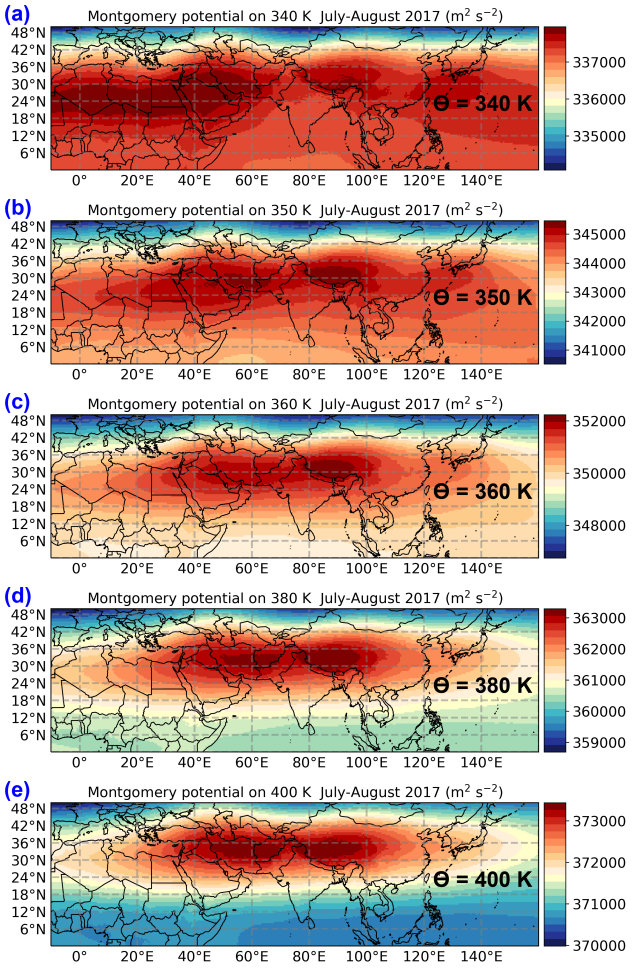

Figure S2. Average Montgomery potential during Jumy-August 2017 on five isentropic levels (a) 340 K, (b) 350 K, (c) 360 K, (d) 380 K and (e) 400 K

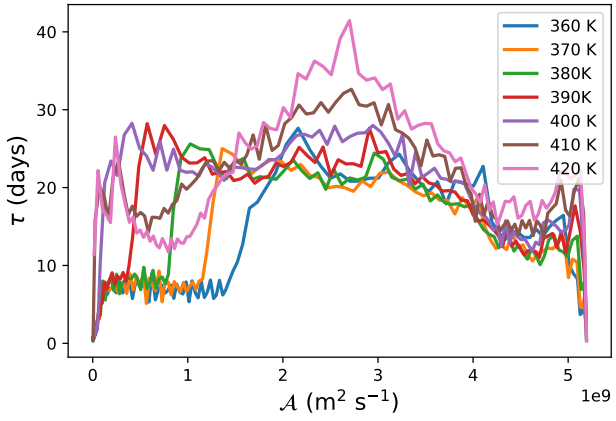

Figure S3. Circulation time calculated form (1) as a function of $\mathcal{A}$ for potential temperatures from 360 K to 420 K.

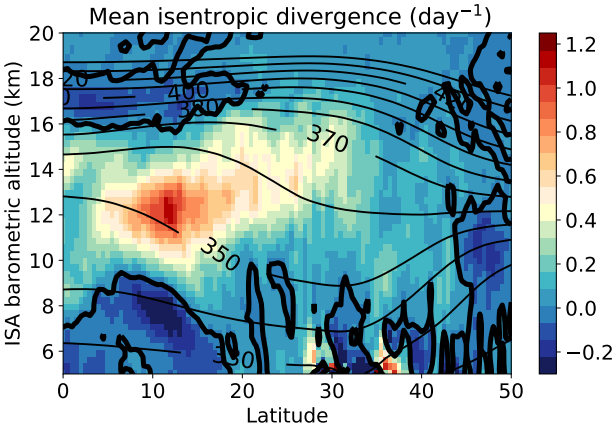

Figure S4. Horizontal isentropic divergence (in $\mathrm{day}^{-}1$) averaged over July-August 2017 in the 73°E-97°E longitude range. Thick contour shows the line of zero divergence. Thin contours show potential temperature (in K).

that encompass the whole AMA while the second is for the internal contours around separate centres. At upper levels, 410 K and 420 K, the slower flow generates circulation times of the order of 4 to 5 weeks. Therefore, we find a typical circulation time of 2 to 3 weeks within the AMA for the mean Montgomery potential between 360 K and 400 K. In practice, smaller recirculation times are expected due to the temporal variations of the Montgomery geopotential. Bucci et al. (2019) observe recirculation times of 10 to 20 days inside the AMA.

S3 Divergence

Figure S4 shows the horizontal wind divergence of the ERA5 in isentropic coordinates, calculated from the divergence in hybrid η coordinates as

$$\mathrm{div}\boldsymbol{U}|_\theta = \mathrm{div}\boldsymbol{U}|_\eta - \frac{\partial \boldsymbol{U}}{\partial \theta}\cdot\boldsymbol{\nabla}_\eta\theta\,.$$

The nonlinear correction term is calculated from the monthly mean velocities and temperature and therefore lacks the contribution from fluctuations at smaller temporal scales.

The divergence is maximum near 350 K by 12°N–, as a matter of fact over the Bay of Bengal. It is positive everywhere from the equator to 45°N between 340 K and 370 K. It is also positive above these levels between 20°N and 45°N. As noticed by Garny and Randel (2013), the divergence is a forcing for the AMA which exhibits maximum jets near the level of maximum divergence.

S4 Normalized cumulated impact

Figure S5 shows the same information as Fig. 5 after normalizing the distribution by its time integral over each level. The normalized impact then becomes a age spectrum for

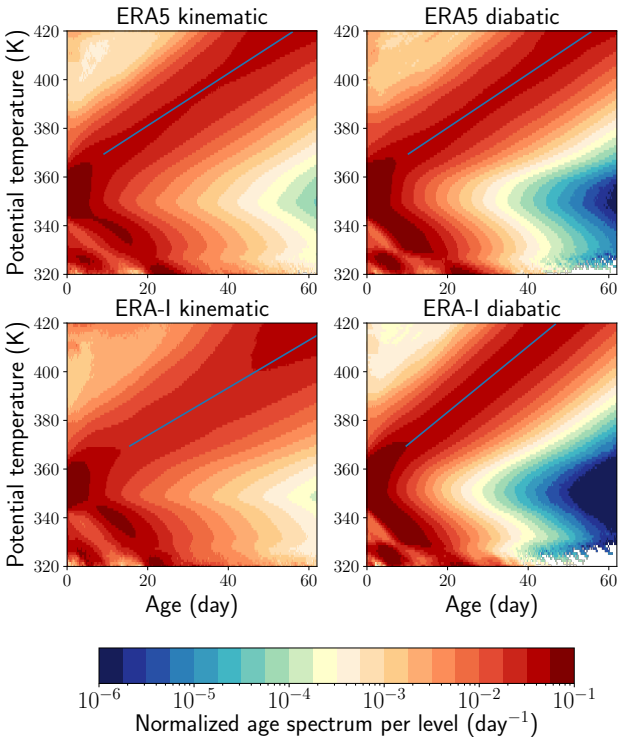

Figure S5. Same as Fig. 5 but after normalizing the distribution on each isentropic level. The slopes are plotted as a fit to the crest above 370 K. They are, respectively, 1.08, 1.11, 0.97 and 1.35 K day^{-1}, for EAZ, EAD, EIZ and EID

each level. The slopes fit the modal age at each level between 370 K and 420 K. In the simplified model presented in Sect. S9 below, this slope is identical to the mean ascent rate.

S5 Longitudinal sections of radiative heating and vertical velocities as heating

Figure S6 shows longitudinal sections of the all sky radiative heating rate and of the Lagrangian potential temperature tendency induced by kinematic motion. We see in the upper right panel that the level of zero radiative heating (LZRH) is fairly flat near 358K at 15°N except localized drops due to clouds, over the Bay of Bengal by 85°E, the Sea of China near 110°E and the Red Sea by 40°E. The LZRH is higher at 30°N (upper left panel) and bulging over the Tibetan plateau with a drop between 85°N and 105°E, but always above the LZRH at 15°N. We also see an intensification of the tropospheric descent in the West of the domain over the African and Arabian deserts.

The Lagrangian potential temperature tendency induced by the kinematic motion (lower panels) is calculated as

$$\frac{D\theta}{Dt}_{\rm kin} = \omega \frac{\partial \theta}{\partial p} + \boldsymbol{U} \cdot \boldsymbol{\nabla}|_p \theta \,,$$

where $\omega = Dp/dt$, from the monthly mean archive of ERA5. This estimate therefore ignores the fluctuating component in the second term of the right hand side. This tendency is much noisier than the heating rates. It is positive within the monsoon region in the whole atmospheric column but is negative below 355 K over the deserts where the air is subsiding within the troposphere. The LZRH is quite close to that of the heating rate at 15°N and does not show any rise at 30°N.

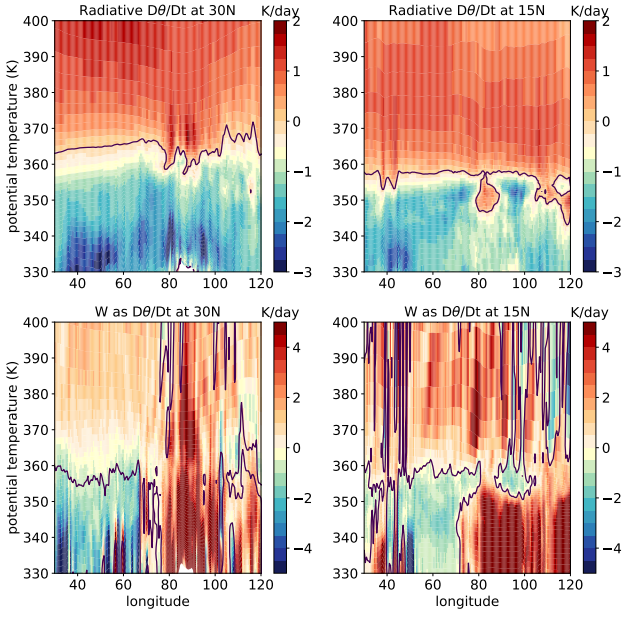

Figure S6. Upper row: vertical section of the all-sky radiative heating rate $d\theta/dt$ averaged over July-august 2017 at 30°N (left) and 15°N (right). Lower row: vertical section of the Lagrangian potential temperature tendency induced by the vertical and horizontal kinematic motion.

S6 Impact and source for ERA5 in the FullAMA domain

Figure S7 compares the equalized impact, as defined in Sec. 2.5 ,for the diabatic and kinematic experiments using ERA5 in the FullAMA domain. The two calculations differ strongly at the lowest level 340 K (panels a and b) where the lack of kinematic descent in the monsoon region generates a low impact centre over the Bay of Bengal (panel b). The descending monsoon branch in the diabatic calculations coupled with horizontal transport also generates impact south of 12°N in Africa which is absent in the kinematic calculations. Both calculations generate descent and impact over Iran, Arabia and the Sahara. This monsoon deficit is still visible at 350K (panels c and d) although it is shifted northward with respect to 340 K and the two patterns are much closer. At higher levels, 360 K and above (panels e to l), the patterns are essentially similar in both calculations, and the isolines

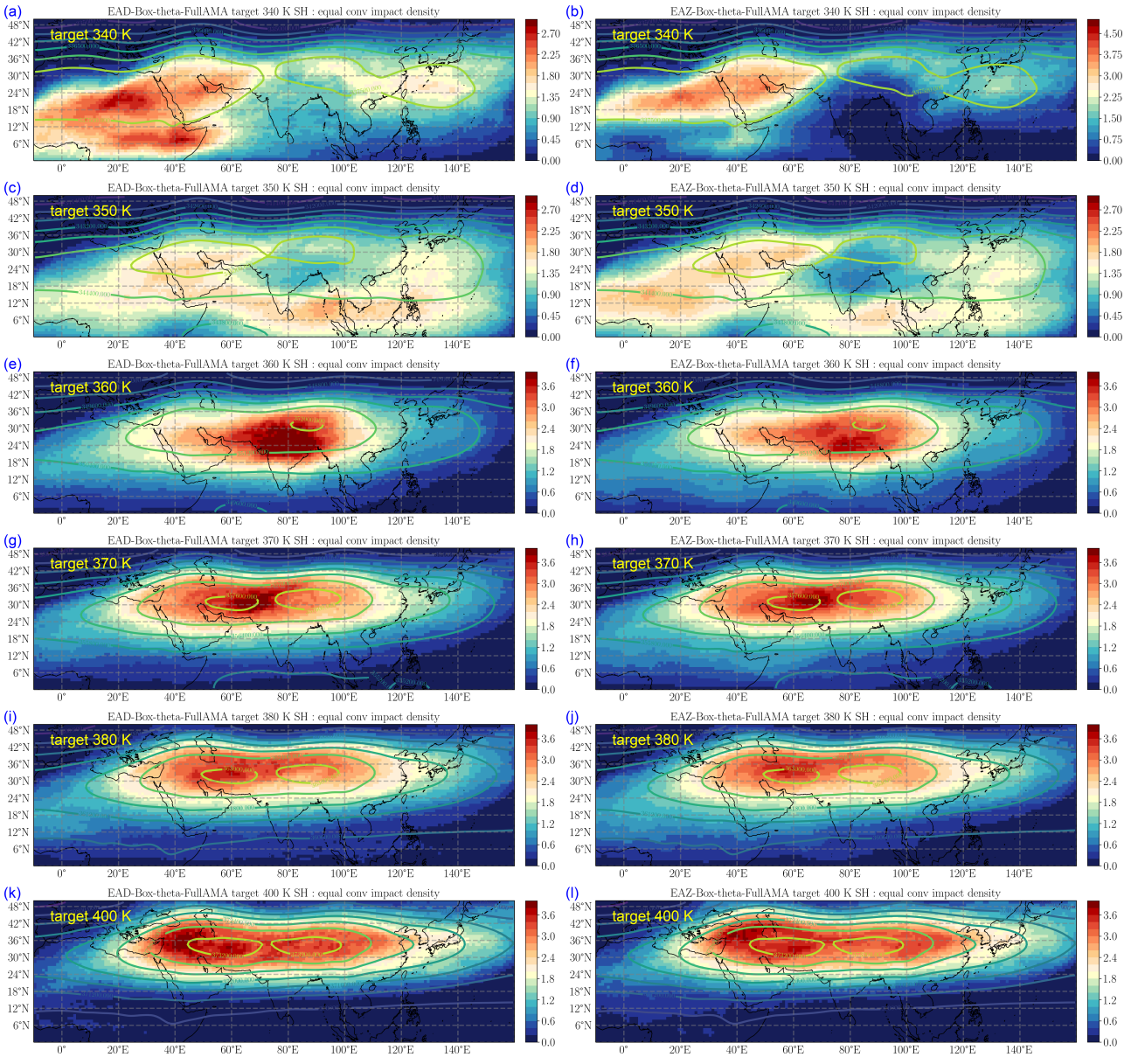

Figure S7. Distribution of the equalized impact for EAD (left column) and EAZ (right column) at potential temperatures 340 K, 350 K, 360 K, 370 K, 380 K and 400 K. The superimposed contours are those of the Montgomery potential at the same levels averaged over July-August 2017.

of the impact follow quite closely that of the Montgomery potential, except near the maxima. The distribution in the diabatic case at 360 K is more compact than in the kinematic case (panels e and f).

The distribution of sources for the same levels, shown in Fig. S8, is very similar in the diabatic and kinematic calculations. There are, nevertheless, a few differences: the contributions of the Indian subcontinent and the Bay of Bengal are reinforced at 340 K in the kinematic case (panels a and b); the contribution from the Sea of China is smaller for the upper levels in the kinematic case.

S7 Impact and source for ERA-Interim in the global domain

In the global domain with ERA-Interim calculations, Fig. S9 corroborates the results shown for ERA5 in Fig. S7. At 340 K, the global ERA-Interim diabatic impact (Fig. S9(a)) closely follows the FullAMA diabatic impact of Fig. S7(a). The kinematic impact shown in Fig. S9(c) exhibits a clear separation and a fairly good symmetry between the two hemisphere with a strong component near 18°S that corresponds to the descending branch of the Hadley circulation

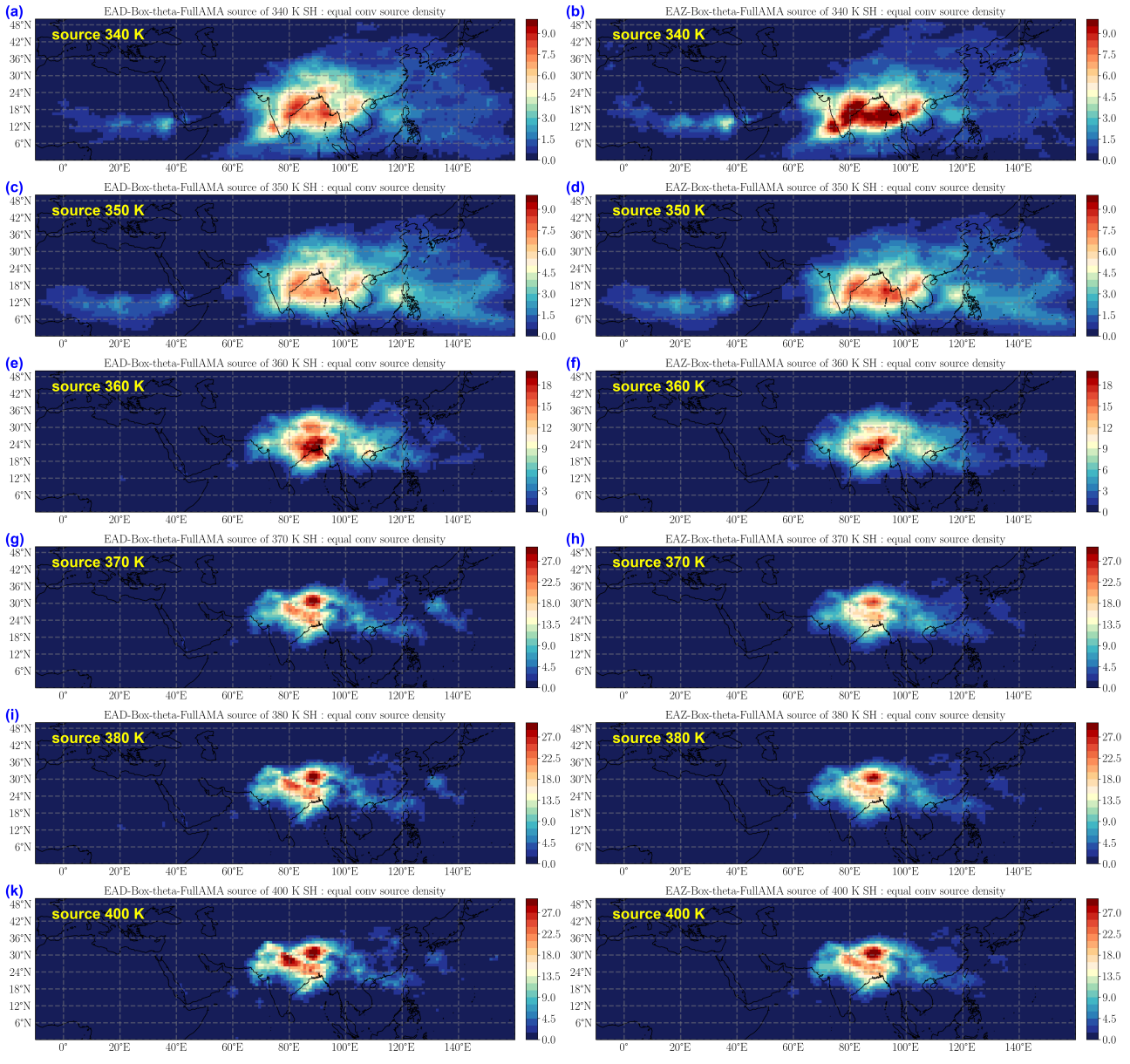

Figure S8. Distribution of the equalized sources for EAD (left column) and EAZ (right column) at potential temperatures 340 K, 350 K, 360 K, 370 K, 380 K and 400 K.

in the Southern hemisphere. This component is present but much more diffuse in panel (a) where most of the impact remains in the northern hemisphere. The part of impact within the FullAMA domain remains close to that of Fig. S7(b).

At 350 K (Fig. S9(c-d)), the ERA-Interim global impact pattern still fits closely that of the FullAMA calculations for ERA5 in Fig. S7(c-d) but for a deeper depletion over the monsoon region in the kinematic case. A strong impact is still visible outside the FullAMA region, especially for the kinematic case.

At 360 K and above, the impact is dominated by the now familiar confinement within the FullAMA region which exhibit a very similar pattern for both cases and when compared to the ERA5 calculations in the FullAMA domain.

It is, however, obvious that the confinement gets reduced with altitude as more and more parcels are leaving the FullAMA domain.

The distribution of sources, shown in Fig. S10 is extremely close between diabatic and kinematic cases at 340 K and 350 K (panels a-d). It remain close at higher levels but the diabatic calculations exhibit a larger contribution of the maritime convection than the kinematic calculations. When compared to Fig. S8, it is clear that the maritime contribution to the impact in the global domain is much larger than for the

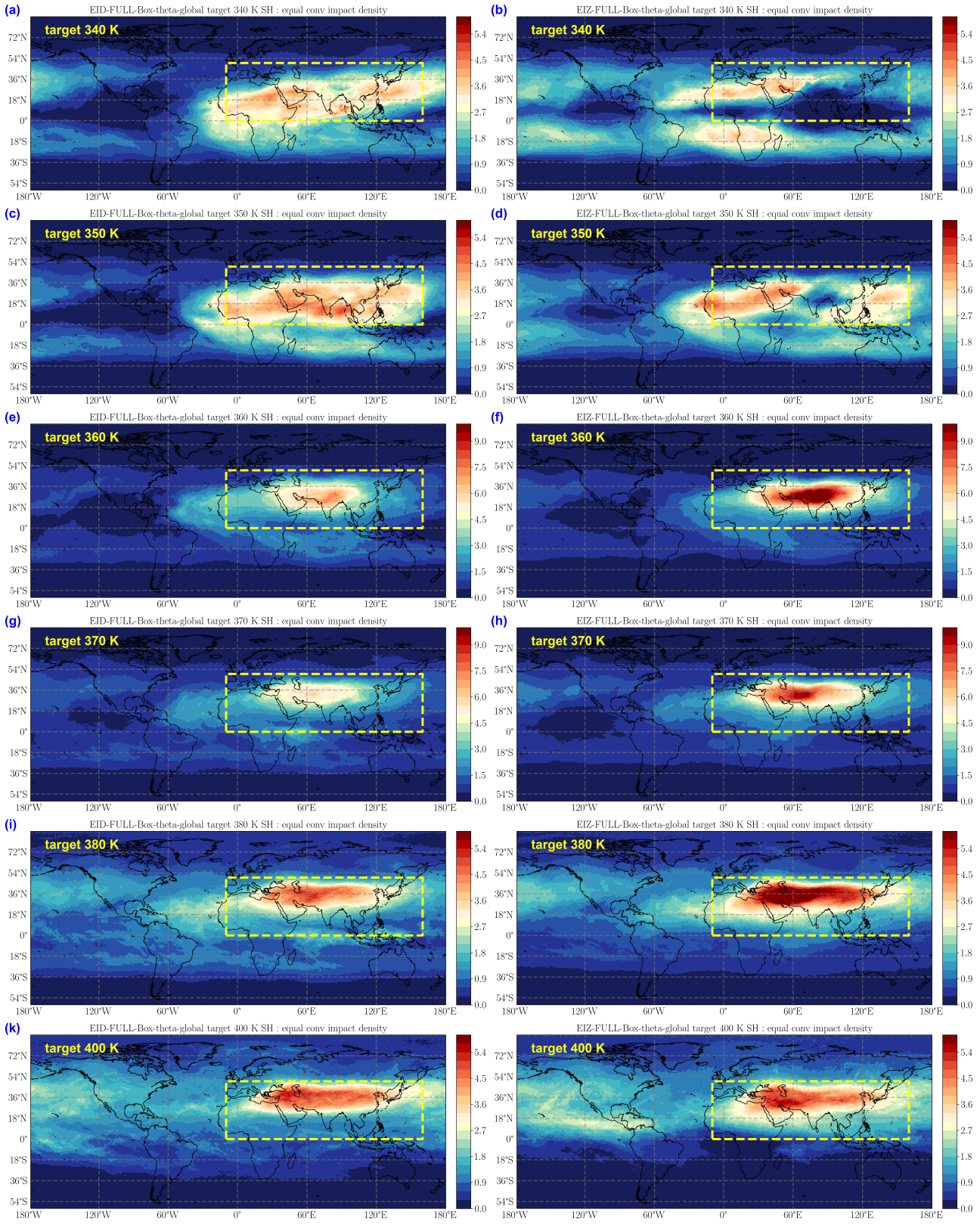

Figure S9. Distribution of the equalized impact for EID-FULL (left column) and EIZ-FULL (right column) at potential temperatures 340 K, 350 K, 360 K, 370 K, 380 K and 400 K. The dashed box indicate the FullAMA domain.

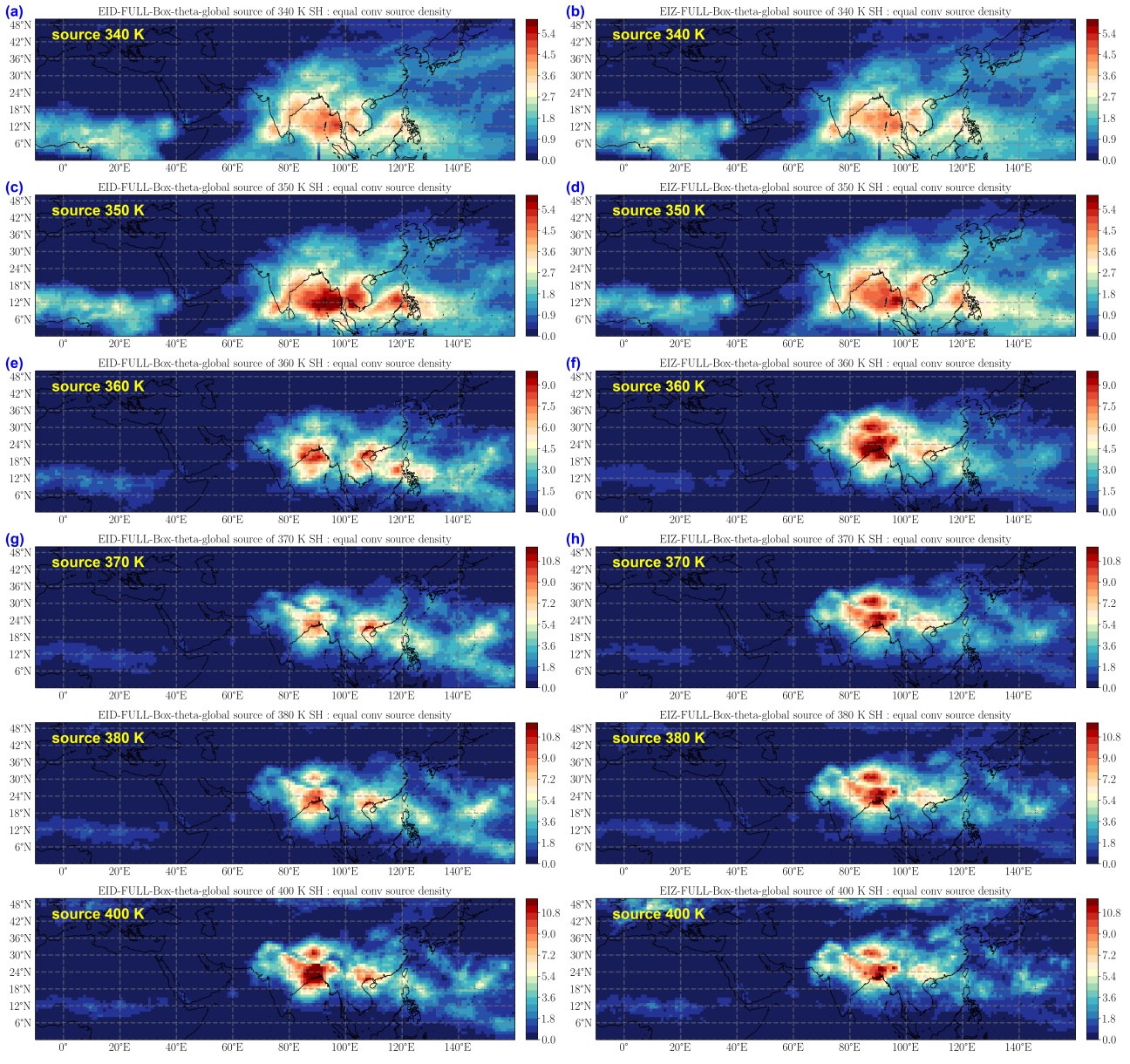

Figure S10. Distribution of the equalized sources for EID-FULL (left column) and EIZ-FULL (right column) at potential temperatures 340 K, 350 K, 360 K, 370 K, 380 K and 400 K. The dashed box indicate the FullAMA domain.

FullAMA impact (see aso Table 1). This is due to the fact that trajectories from maritime sources travel rapidly along the jets at the periphery of the AMA, in particular the southern easterlies, do not penetrate within the core and exit also rapidly across the boundaries.

S8 Age for the backward calculations

Figure S11 shows age distribution for the backward calculations. At 360 K and above (Fig.S11(c-h)) the age pattern closely follows that of the forward calculation both in the target and the source spaces. The backward age value is slightly smaller than the forward age because only the first backward encounter is accounted.

S9 Advective-loss 1-D model with idealized heating and sources

The solution to (1) of the main text with $\dot{\theta} = \Lambda(\theta - \theta_0)$ for $\theta_0 < \theta < \theta_1$, $\dot{\theta} = A = \Lambda(\theta_1 - \theta_0)$ for $\theta > \theta_1$ and $S(\theta) = S_0 e^{-\beta(\theta-\theta_0)}$ is

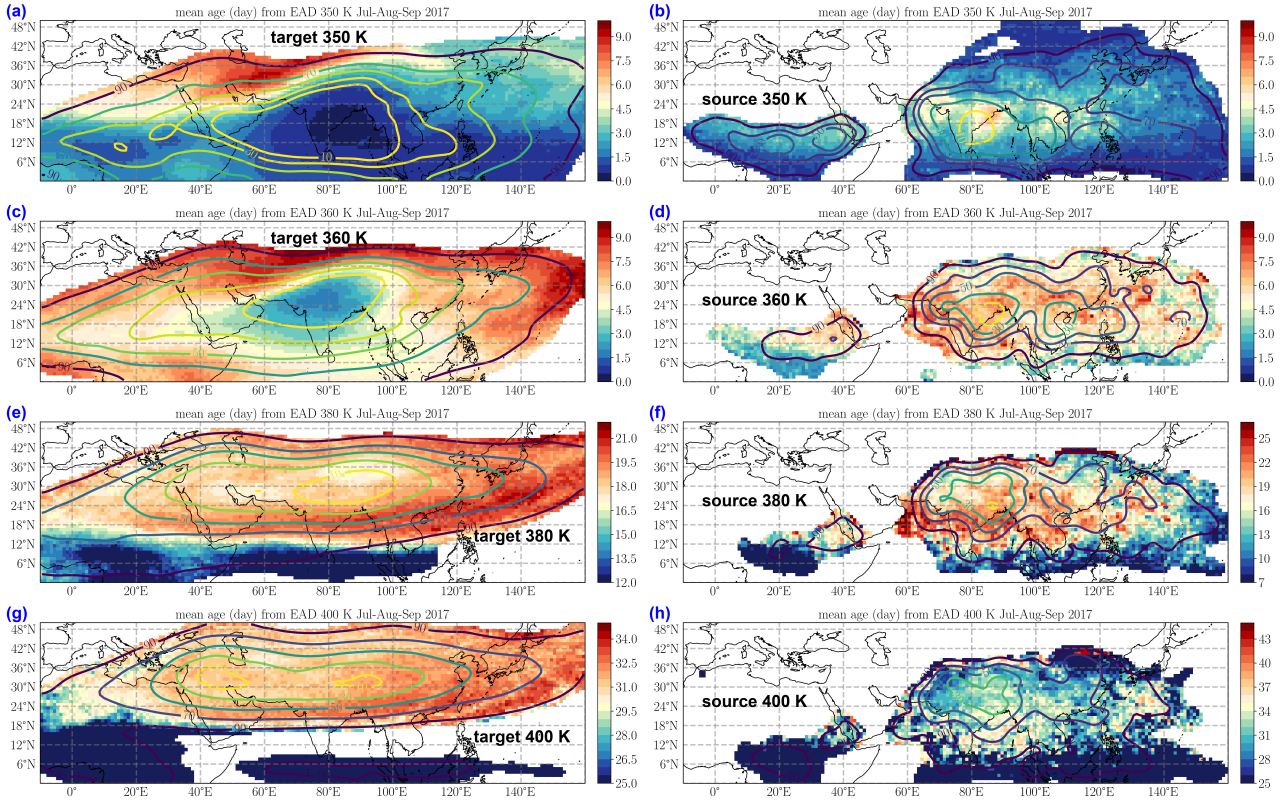

Figure S11. Left column (a,c,e,g): mean age with respect to convection for backward parcels hitting a convective cloud at 350 K (a), 360 K (c), 380 K (e) and 400 K (f). Right column (b,d,f,h): mean age in the source domain for the same parcels as in the left column for each level.

for $\theta < \theta_1$:

$$F(\theta,t) = S_0 \exp\left\{-(\alpha+\Lambda)t - \beta(\theta-\theta_0)e^{-\Lambda t}\right\} \tag{2}$$

for $\theta > \theta_1$ and $t < (\theta-\theta_1)/A$:

$$F(\theta,t) = S_0 \exp\left\{-(\alpha-\beta A)t - \beta(\theta-\theta_0)\right\} \tag{3}$$

for $\theta > \theta_1$ and $t > (\theta-\theta_1)/A$:

$$F(\theta,t) = S_0 \exp\left\{ -\alpha\frac{\theta-\theta_1}{A} - (\alpha+\Lambda)\left(t - \frac{\theta-\theta_1}{A}\right) - \frac{\beta A}{\Lambda}\exp\left[-\Lambda\left(t-\frac{\theta-\theta_1}{A}\right)\right]\right\} \tag{4}$$

This solution is illustrated in Fig. S12 for the basic set of parameters $\theta_0 = 360$ K, $\Lambda = 0.1$ day^{-1}, $\beta = 0.4$ K^{-1} and $A = 1$ K day^{-1}, that mimic the situation for the ERA5 diabatic transport in the monsoon area, as a function of age at the level $\theta = 360$ K. The modal age and mean age are about 30 days in rough agreement with the curve shown on Fig. 7. Figure S12 also shows the effect of changing the parameters by multiplying Λ by 3, β by 0.4, α by 2 and A by 3. It is visible that, for the displayed regime, Λ basically controls the width of the distribution without changing the modal age. Changing α both changes the shape and the modal age. The parameter β, when reduced, leads to a new regime where the maximum is attained at $t = (\theta-\theta_1)/A$; when increased or less decreased (not shown), the effect reduces mainly to a translation in time. A performs essentially a translation in time.

The full range of the parameters can be thoroughly explored with interactive plots provided in the accompanying Mathematica CDF notebook that can be played using the free Wolfram player.

S10 Variability of the impact during the summer season

In order to dwell on the variability of the impact during the monsoon season, Fig. S13 shows a sequence of charts for five decades of arrival time at 380 K from July 11 to August 31, 2017. There are significant variations in the detailed distribution of the impact with temporary sharp concentrations within filamentary structures. However, the main pattern remains that of the seasonal mean shown on panel (f). Figure S14 shows the variation of the cumulated impact per day over the season for levels between 340 K and 410 K. In the right panel, the curves have been normalized and shifted

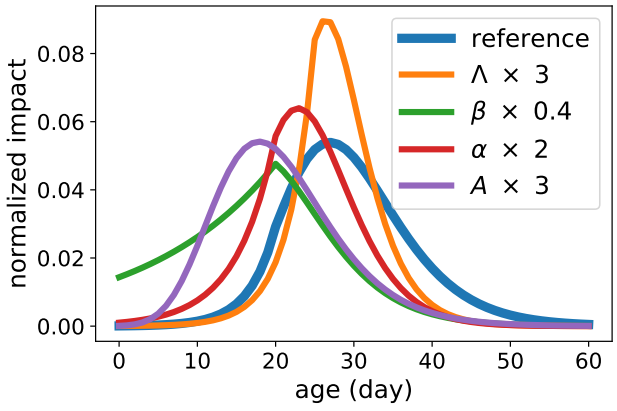

Figure S12. Solution of (1) described by (2-4) for the parameters given in the text and modified solutions according to the changes indicated in the legend. Each curve is normalized with respect to its integral in the displayed interval.

to show better the vertical propagation. During the first half of August, the propagating signal from 370 K to 390 K follows the slope of the mean ascent in this region. At 380 K and above, a break occurs at the beginning of August as the loss from the FullAMA domain temporally increases, while the confinement temporarily increases in the lower levels below 370 K .

References

Bucci, S., Legras, B., Sellitto, P., D'Amato, F., Viciani, S., Montori, A., Chiarugi, A., Ravegnani, F., Ulanovsky, A., Cairo, F., and Stroh, F.: Deep Convective Influence on the UTLS Composition in the Asian Monsoon Anticyclone Region: 2017 StratoClim Campaign Results, Atmospheric Chemistry and Physics Discussions, p. submitted, 2019.

Garny, H. and Randel, W. J.: Dynamic Variability of the Asian Monsoon Anticyclone Observed in Potential Vorticity and Correlations with Tracer Distributions, Journal of Geophysical Research: Atmospheres, 118, 13,421–13,433, https://doi.org/10.1002/2013JD020908, 2013.

Nakamura, N.: Modified Lagrangian-Mean Diagnostics of the Stratospheric Polar Vortices. Part I. Formulation and Analysis of GFDL SKYHI GCM, Journal of the Atmospheric Sciences, 52, 2096–2108, https://doi.org/10.1175/1520-0469(1995)052<2096:MLMDOT>2.0.CO;2, 1995.

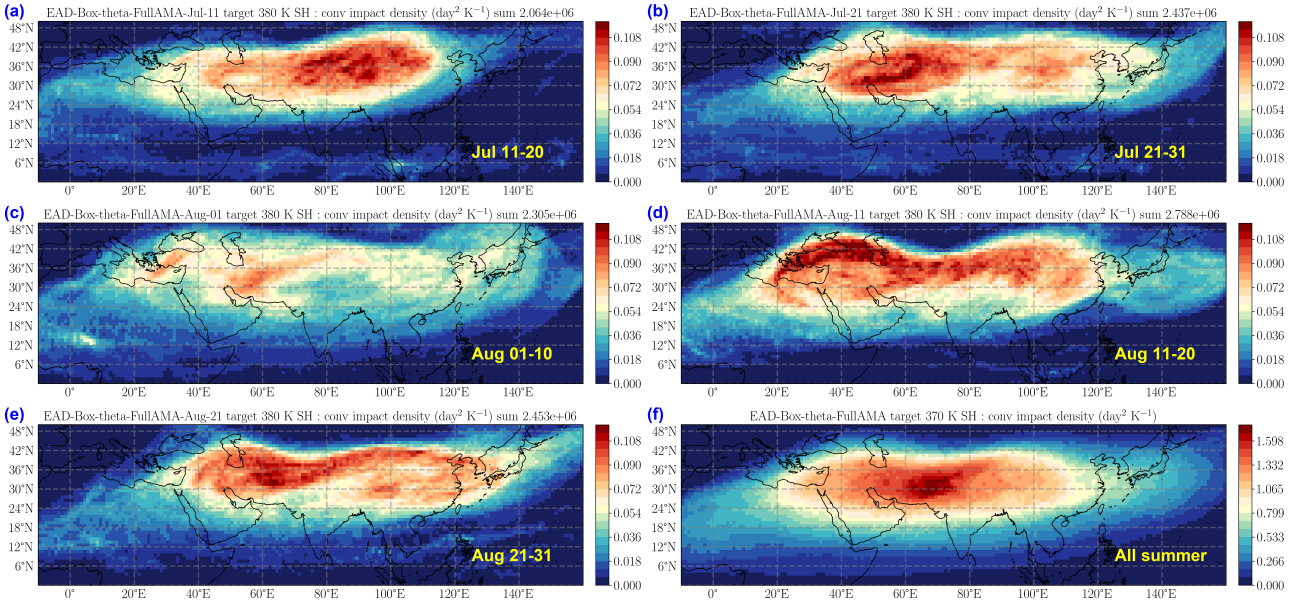

Figure S13. Impact density at 380 K for forward trajectories of ages less than 40 days reaching that level within the decades July 11-July 20 (a), July 21-July 30 (b), Aug 1 - Aug 10 (c), Aug 11 - Aug 20 (d), Aug 21 - Aug 30 (e) and for the whole summer (f).

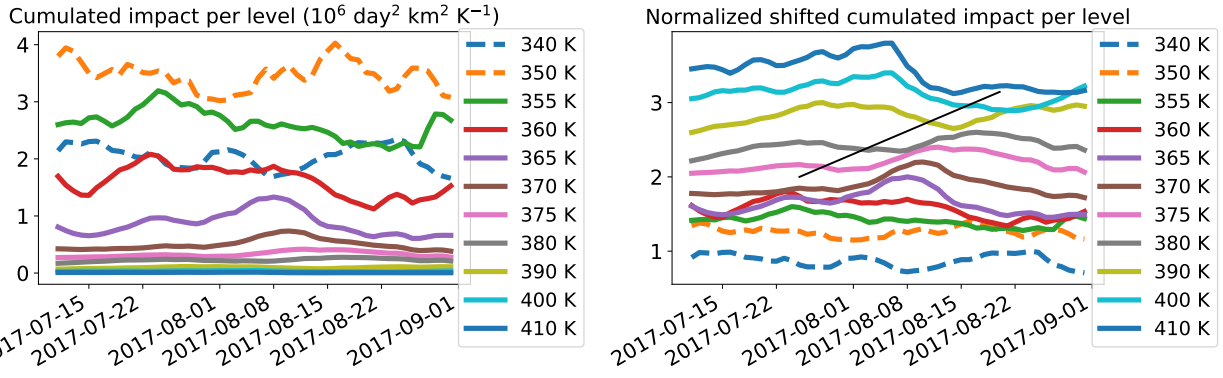

Figure S14. Upper panel: cumulated daily impact per level for parcels with age less than 40 days for the nine levels from 340 K to 410 K listed in the legend. Lower panel: same curves but each normalized by its maximum value over the shown time interval and shifted by $0.04 \times (\theta - 340)$ where θ is the potential temperature in K. Therefore the curves are in increasing order from the bottom according to θ. The black line shows the slope corresponding to a heating rate of 1.1 K day^{-1} that fits the ERA5 diabatic mean ascent (see Fig.5).